On the Effects of the External Surface on the Equilibrium Transport in Zeolite Crystals

N. E. R. Zimmermann,[*,†] B. Smit,[‡] and F. J. Keil[†]

Chemical Reaction Engineering, Hamburg University of Technology, Eissendorfer Str. 38, 21073 Hamburg, Germany, and Department of Chemical Engineering and Department of Chemistry, University of California – Berkeley, 1018 Gilman Hall, Berkeley, CA 94720-1462, USA

E-mail: nils.zimmermann@tu-harburg.de

[†]Hamburg University of Technology
[‡]University of California – Berkeley

Abstract

With the aid of molecular simulation techniques (molecular dynamics [MD], Grand-Canonical Monte Carlo [GCMC], and reactive flux correlation function [RFCF]), the influence of the external surface on the equilibrium permeation of methane and ethane into and out of an AFI-type zeolite crystal has been studied. In particular, “extended dynamically corrected transition state theory”, that has been proven to describe the transport of tracers in periodic crystals correctly, has been applied to surface problems. The results suggest that the molecules follow paths that are close to the pore wall in the interior, and also at the crystal surface. Moreover, the recrossing rate at the surface turns out to be non-negligible, yet, in contrast to the intracrystalline recrossing rate, remains almost constant over loading which gives indication to diffusive barrier crossing at the crystal surface. As a consequence of very different adsorption and desorption barriers, the corresponding permeabilities are shown to be not equal for one and the same condition (T, p). The critical crystal length, beyond which surface effects can be certainly neglected, is computed on basis of flux densities. Entrance/exit effects, in the present cases, are practically important solely for ethane at low pressures. The influence of the type of external surface on the surface flux is, hereby, rather small, because the transport at the surface is controlled by the slow supply from the gas phase. This has been evidenced by a simplified thermodynamic model that has been derived within this work and which is based on rapidly assessable simulation data. Finally, we propose a procedure for estimating the importance of different factors that have an impact on surface effects.

Keywords: diffusion, surface barrier, nanopore, simulation, TST.

1 Introduction

Nanoporous materials, such as zeolites, metal-organic frameworks (MOFs), and carbon nanotubes (CNTs), represent a very important class of solid materials. In some cases, they have already made a significant industrial impact (zeolites). In other cases, their peculiar properties make them a promising candidate for novel applications (MOFs and CNTs). Using the example of zeolites, that have a long research history, one can grasp to which extent nanoporous materials can be potentially used. Starting with rather simple adsorption for gas separation (N_2-O_2 separation), over ion-exchange processes (water softening), to heterogeneously catalysed reactions (cracking of alkanes), only the most well-known applications of zeolites are listed. However, they may even be used for microelectronics and medical diagnosis[1], and have the potential to serve as permenant medical material to be implanted into human bodies.[2] The latter two applications crucially depend on a very good understanding of adsorption and diffusion of condensed matter into and out of the zeolite crystals.

Although zeolites have been focus of innumerable works addressing adsorption, transport, and reaction issues of adsorbed matter, there is still considerable confusion even about the simpler processes of adsorption and transport inside the micropores. Consider for example diffusion: although it seems that, by now, fluid diffusion in the pores of zeolite crystals is understood quite well, e.g. see Refs. 3–5 and references therein, there is still a lack of understanding why and for which adsorbent-adsorbate systems so-called surface effects have a crucial impact on the permeation into and out of the crystals. These effects are speculated to be one of the most prominent reasons to why diffusion coefficients obtained from macroscopic methods, e.g. uptake experiments, and microscopic methods, e.g. pulsed-field gradient NMR (PFG-NMR), and quasi-elastic neutron scattering (QENS), sometimes deviate tremendously for one and the same system.[6] Recent works of the group of Jörg Kärger using the interference microscopy (IFM) technique indicate that there are systems which exhibit tremendous surface effects whilst other systems are entirely controlled by slow intracrystalline diffusion.[7,8] The IFM technique makes use of the refractive index of the zeolite+adsorbate system which directly correlates to the prevailing loading inside the

zeolite crystal,[7] so that 2-dimensional concentration profiles can be measured transiently. In spite of the relatively high spatial resolution of the concentration profiles (approx. $0.5 \times 0.5\ \mu m^2$), it is difficult to trace the reasons to why surface barriers occur for a given adsorbent-adsorbate system on basis of IFM. Owing to their detailed insights simulations can help finding those reasons and, in the best case, provide a mechanism, hence complementing the experimental observations made, e.g. why no surface barriers are observed by IFM, or why they are very large.

Several molecular simulation studies have been conducted that have investigated the effect of external surfaces on the adsorption and desorption of fluids.[9–15] On basis of molecular dynamics (MD) simulations Schüring *et al.*[10] have observed that, for neopentane-like systems, the condition of single-file diffusion leads to an accelareated surface exchange rate but to a slower intracrystalline exchange. Gulìn-Gonzàlez *et al.*[11] performed MD tracer-exchange experiments of a small heavy Lennard-Jones fluid leaving an $AlPO_4$-5 crystal. From their results they suggest that large potential energy differences between the intracrystalline and intercrystalline space cause the tracer-exchange profiles along the pores of small crystals to be flat. This indicates a large surface transport resistance. Since the profiles get more curved as the crystal size increases, the influence of the surface transport levels off with increasing crystal size. Arya *et al.*[12] have studied methane permeation through an $AlPO_4$-5 crystal using dual-control volume Grand-Canonical MD (DCV-GCMD) simulations and equilibrium MD simulations. They have shown that the effect of external surface barriers diminishes as temperature and loading increases. On basis of a simple activated transport model they have furthermore shown that the surface effect is more pronounced for large molecules, i.e., when the ratio of molecule size to pore size approaches unity. Newsome and Sholl[13,14] confirmed these general observations for various fluids through a silicalite crystal and proposed an own method that uses quantities that can readily be accessed from equilibrium MD simulations for predictively assessing the importance of surface effects. Ahunbay *et al.*[15] performed DCV-GCMD simulations of methane through a silicalite crystal and they have observed a coupling between entrance and exit surface resistances, when methane permeates from one gas reservoir (control volume 1) through the crystal to another gas reservoir at the opposite side of the

crystal (control volume 2). When the resistances are computed by separate simulations, i.e., one control volume is located inside the bulk gas phase and the other one inside the zeolite, it turns out that the resistance to adsorption is stronger than that to desorption.[15] It should be noted here that Arya *et al.* have shown that DCV-GCMD simulations can severely suffer from technical issues such as not adding streaming velocities on newly inserted molecules and choosing a low ratio of stochastic to deterministic steps.[16]

Some of the works mentioned above have computed *equilibrium* fluxes at the external crystal surface. These were either computed by counting the molecules passing a pre-defined plane that separates gas phase and zeolite space, or the fluxes were computed on the basis of adsorption/desorption rates via free/potential-energy profiles. In either case, a phenomenon is usually disregarded that has been shown to be of great significance to self diffusion of gas molecules inside the *bulk* zeolite: the so-called recrossing events.[3–5,17] Recrossing events stem from viewing the self diffusion of adsorbates in zeolites as a random walk on a lattice. A molecule can jump from one adsorption site to an adjacent one at a rate that is determined by two factors: the free-energy barrier that impedes the jump and the likelihood that a jump *attempt* is eventually successful. The second factor, that is, in most cases, a function of zeolite loading, is mainly influenced by these recrossing events which decrease the probability of successful jumps. The theory that comprises the underlying physics is known as “dynamically corrected transition state theory” (dcTST). We, therefore, use dcTST in this paper in order to compute equilibrium transport rates of methane and ethane inside the micropores and at the external surface of an all-silica AFI-type zeolite crystal to eventually assess the importance of surface effects on the permeation of adsorbates into and out of the crystal.

The remainder of this work is structured as follows. In section 2, the methodology of this work is described. Apart from modeling details (subsection 2.1 and 2.2), the main ideas behind “extended dynamically corrected transition state theory” are presented (subsection 2.3). The results are subsequently presented and discussed (section 3). The last section concludes the results from a broader point of view.

2 Methodology

2.1 Zeolite description and simulation box

The zeolite under investigation was a purely siliceous AFI-type which exhibits parallel pores without interconnections. As experienced by methane molecules, the pores are slightly corrugated. Narrower regions with a diameter of approximately 7.3 Å (called windows in the following) are followed by wider regions of a diameter of ≈10.0 Å (called cages), see Figure 1. The windows are formed by a ring of 12 oxygen atoms where 2 O-atoms are connected through one and the same silicon atom. A single unit cell consists of 96 oxygen and 48 silicon atoms, and its dimensions are 23.774 Å, 13.726 Å, and 8.484 Å in *x*, *y*, and *z* direction, respectively. The original crystal structure, as taken from Ref. 18, was converted from monoclinic to orthorhombic for computational efficiency and thus accomodates 4 cages in total.

The crystals were aligned in (0 0 1) direction (Cartesian *z* directon). The simulation box included 2 unit cells in *x*, 3 in *y*, and 4 in *z* direction which were centered in the simulation box. In addition, fractional unit cells, that were cleaved perpendicular to *z*, were "glued" on the last unit cells in *z*-direction. Two conceptually different truncations were chosen for one and the same simulation box:

1. On the negative *z* side of the zeolite plate, the window O-atoms formed the outmost zeolite atoms, and

2. on the positive *z* side, those 6 oxygen atoms that form the center of the cages concluded the crystal.

This methodology allowed us to study the role of the truncation plane systematically.

As can be seen by Figure 1 (bottom), the crystal accommodates 10 full cages. The length of the zeolite space in *z* direction, as measured by the position of the outmost oxygen atoms on either side, was 44.4 Å; the length of the gas phase was 50 Å. The simulation box consisted thus roughly of 50% zeolite volume and 50% gas volume. Periodic boundary conditions were used in

all directions, creating an infinite repetition (in z direction) of infinitely large (in x and y) zeolite plates and gas chambers. At this point it should be mentioned that past simulation studies labeled comparable systems *zeolite membranes*. However, the results from such molecular simulations rather compare to single-crystal experiments, such as interference microscopy, and infrared microscopy measurements, than to permeation experiments on membranes in the conventional sense of the term membrane. Those usually comprise of a non-zeolitic support layer, and a polycrystalline zeolite film (intergrown grains) that may be covered by an amorphous silica layer depending on the post-synthesis treatment.[19,20] In this context, it is worth mentioning that Caro and Noack have reviewed recent developments and progress of such zeolite membranes.[21]

There is still a lack of knowledge with respect to the molecular structure of the surface of zeolite crystals. For example, cleavage of the zeolite structure will introduce silanol groups (chemical saturation of the external surface) which will have a different structure as compared to the cleaved surfaces considered in this work. This lack of molecular information renders a direct comparison with experimental data difficult. However, in order to gain some insights into the role of the surface, the above described methodology (two different truncation planes) may be considered worthily. Nonetheless, it should be mentioned that, only recently, Thompho *et al.*[22] have introduced a potential for such silanol groups on a silicalite-1 surface, and that future studies should take into account the surface saturation. Another important point with respect to studying a realistic crystal are lattice defects,[23] and crystal intergrowth,[24] all of which are not considered in this study but which are very likely be found in real zeolite crystals. From another point of view, this underlines the complementary relationship between experiments and simulations. As soon as there will be experimental data of the systems under investigation, those influences may be estimated from the comparison between simulation data using highly idealized crystals and experimental results where non-idealities certainly occur.

2.2 Simulation details

We have performed molecular dynamics (MD) simulations in the NVT ensemble whereby the crystal structure was held rigid for reasons of computational efficiency and structural concerns.[25] The Lowe-Andersen thermostat for interface-fluid collisions[26] (LA-IFC) was used in order to maintain the temperature during the production phase. This thermostat mimics the energy exchange between vibrating pore atoms and adsorbate molecules *correctly for carbon nanotubes*.[26] As for zeolites, there are no parameters available. Therefore, the collision frequencies were estimated from published carbon nanotube (CNT) simulations.[27] The frequencies do, in fact, not vary much for methane in CNTs whose radii are of similar size as the mean AFI pore radius.[28] Note that, due to the corrugation of the AFI pore wall, the region to be thermalized (on basis of $r_{\mathrm{LA-IFC}}^{\mathrm{cutoff}}$) is not a cylindrical shell, as was the case for the smooth CNTs. Rather explicit adsorbate-zeolite atom distances are determined for testing if an adsorbate is in thermalizing distance to *a* zeolite atom and the Verlet lists of the energy and force calculation help speeding up this search.

Tests in a periodic AFI crystal revealed that, at zero loading, perturbing the choosen frequencies by a factor of 2 does not lead to different self-diffusivities. The collision frequency was set to $\Gamma = 10^{11}/\mathrm{s}$, this is, equal thermalization in all directions, and the cutoff radius was set to 3.6 Å. A final comparison between the LA-IFC thermostat and the Nosé-Hoover chain thermostat[29] in a periodic AFI crystal (see Figure 1 in the Supporting Information) shows that both the free-energy profile along the diffusion direction z and the mean-squared displacement (MSD) do not differ. Finally, all simulations were performed at a temperature of 300 K.

Methane and ethane were modeled as CH_x beads of united atoms. The force field of Dubbeldam *et al.*[30,31] was used for adsorbate-adsorbate and adsorbate-zeolite interactions. This force field was specifically developed to reproduce adsorption isotherms of alkanes in zeolites accurately. In addition, Beerdsen and Smit[32] have shown that this force field even yields a good description of the loading dependence of the methane self-diffusion coefficient in MFI. The silicon atoms were assumed to be shielded by the large oxygen atoms. For ethane, an additional harmonic potential was used to model the intramolecular vibration of CH_3-CH_3 beads. The potential parameters are

given in Table 1. The Lennard-Jones potentials were cut at a distance of 12 Å and shifted in order to avoid singularities in potentials and forces.

Newton's equations of motion were integrated numerically using a standard velocity-Verlet algorithm and a time step of 1.0 fs for methane and 0.5 fs for ethane simulations, respectively. A Monte Carlo initialization phase of several thousand translational and rotational moves (the latter only for ethane) as well as a velocity-scaling MD phase (≈100 ps) with final equilibrium NVE-MD phase (≈1 ps) preceded the production runs.

2.3 Extended dynamically corrected transition state theory

Several recent publications showed that the self diffusion of molecules adsorbed in zeolite materials can be accurately computed by the approach of extended dynamically corrected transition state theory[3–5,17] (extended dcTST). As the self-diffusion coefficient, D_S, is, in general, a function of loading for a given adsorbate-zeolite system at a given temperature, extended dcTST provides a valuable means to discuss the loading dependence of D_S on the basis of those two factors that comprise the theory:

1. **Free-energy contribution** (static property). Usually, one of the Cartesian directions is identified as the reaction coordinate, q, that measures the progress of a jump event from reactant state, q_A, over the transition state, $q^\ddagger$, toward the product state, q_B; in this work $q = z$. Free-energy profiles along the reaction coordinate, $F(q)$, are calculated from residence histograms of a tagged adsorbate molecule, as obtained from the simulations. Finally, the relative probability, $P_{\in A}(q^\ddagger)$, to find the molecule on top of the barrier is computed

$$P_{\in A}(q^\ddagger) = \frac{e^{-\beta F(q^\ddagger)}}{\int\limits_{\text{cage A}} e^{-\beta F(q)} dq}. \tag{1}$$

2. **Flux through dividing surface** (dynamic property). The idealized TST flux through the dividing surface at $q^\ddagger$ is approximated by kinetic gas theory, such that the jump frequency

from A to B, $k^{\mathrm{TST}}_{\mathrm{A}\to\mathrm{B}}$, reads

$$k^{\mathrm{TST}}_{\mathrm{A}\to\mathrm{B}} = \sqrt{\frac{k_{\mathrm{B}}T}{2\pi m}} \cdot P_{\in\mathrm{A}}(q^{\ddagger}). \tag{2}$$

k_{B} is Boltzmann's constant, T the absolute temperature, and m the mass of the bead(s), or atom(s) involved in the reaction coordinate (in this work: center-of-mass of entire molecule). Spurious crossings are accounted for by taking the plateau value of the reactive flux correlation function[4,33,34] (RFCF), $\kappa(t)$,

$$\kappa(t) = \frac{\left\langle \dot{q}(0) \cdot \mathrm{H}[q(t) - q^{\ddagger}] \cdot \delta[q(0) - q^{\ddagger}] \right\rangle}{\left\langle 0.5 \cdot |\dot{q}(0)| \right\rangle}, \tag{3}$$

where $q(0)$ and $\dot{q}(0)$ denote the initial position and velocity of the molecule, respectively. H is the Heaviside function ($\mathrm{H}(x) = 1$ for $x \geq 0$ and $\mathrm{H}(x) = 0$ otherwise). Starting configurations for the RFCFs were generated using an MD-based approach (BOLAS[35], EPS[36]). Otherwise, the procedure for the RFCF simulations is the same as in Ref. 4.

The methodology describe above is also known as the Bennett-Chandler approach.[33,34] It has been often used in order to understand diffusion in nanopores at the limit of infinite dilution, see for example the numerous references in Ref. 4. The key to extending dcTST to diffusion at finite loadings is the computation of *effective* hopping rates of a *single* tagged molecule. Surrounding adsorbate molecules are viewed as an additional external field to the tagged molecule, and naturally fluctuating cage occupancies are crucial to the hopping rate computed.[3] In fact, this viewpoint is similar to what Chandler[34] anticipated for the isomerization of *n*-butane: the rate constant would strongly depend on the solvent density that excerts an external field to *n*-butane.

The self-diffusion coefficient, D_{S}, is, on basis of dcTST, calculated by[4,17]

$$D_{\mathrm{S}} = \frac{1}{2d} \cdot \kappa k^{\mathrm{TST}}_{\mathrm{A}\to\mathrm{B}} \cdot \lambda^2, \tag{4}$$

where d denotes the dimensionality of the pore system (here $d = 1$), and λ the separation of hopping sites in the zeolite structure (here λ =4.242 Å). It is the measure for the *intra*crystalline transport of *single* molecules. Transition state theory has recently also been used to characterize equilibrium transport at crystal surfaces.[11,37] However, we are not aware of any crystal surface study that has accounted for the dynamic correction (spurious crossings) which may yet have a profound impact on the surface transport.

In analogy to the surface permeability, α, which describes the mass transport at surfaces under the influence of a driving force ($\Delta\mu$), one can define a tracer permeability at the surface, α_S, for characterizing the extent of transport at the crystal surface under equilibrium conditions, compare also Ref. 11,

$$\alpha_S = \kappa k_{A\rightarrow B}^{TST,surf} \cdot \lambda_{surf}. \tag{5}$$

λ_{surf} denotes the length between the free-energy well on the bulk-gas side of the pore mouth and the well on the zeolite side. The subscript S stresses that this quantitiy is related to single-molecule motion rather than to collective transport.

2.3.1 Critical crystal length

In order to assess the relative importance of surface transport effects, Arya et al. pointed out that any such assessment "... *must include an estimate of the critical crystal dimension beyond which the barrier resistance becomes insignificant*".[12] They have therefore introduced a critical ratio of the two lengths involved, i.e., of the pore length, l^{pore}, to the length of the pore exit region, l^{exit}, and, on basis of a simple activated transport model, provided a good estimate for this ratio. In a similar manner, and also using a simplified equilibrium model, Newsome and Sholl have defined a critical crystal length, L^{crit}.[13,14] Using the example of adsorption, the model of the authors finally reduced to following equation[14]

$$\frac{R_{ads}}{R_{intra}} \approx \frac{D_C(c_{feed})}{\alpha L}\frac{c_{feed}}{P_{feed}}, \tag{6}$$

where R_{ads} and R_{intra} denote the adsorption and intracrystalline transport resistance, respectively, D_{C} the corrected diffusivity, and c_{feed} the concentration inside the zeolite in equilibrium with P_{feed}, the gas-phase pressure outside the crystal. Note that they have defined α as the derivative of the flux density with respect to pressure, $\alpha \equiv \mathrm{d}j/\mathrm{d}P$.

In this study the fact that dcTST originates from chemical reactions, and that the molar flux density, $j_{\text{A}\to\text{B}}$, between two adsorption site thus corresponds to the rate of change of species i, $\mathrm{d}n_i/\mathrm{d}t$, is used for assessing the importance of surface transport effects. The molar flux density in terms of dcTST is given by (compare also Ref. 11)

$$j_{\text{A}\to\text{B}} = \kappa \cdot k^{\text{TST}}_{\text{A}\to\text{B}} \cdot \langle c_{\text{A}} \rangle \lambda_{\text{A}}, \tag{7}$$

$\langle c_{\text{A}} \rangle \lambda_{\text{A}}$ stems from computing the number of species A (found left from the transition state: $\langle n_{\text{A}} \rangle = \int_{\text{cage A}} \langle c \rangle \cdot \mathrm{d}V^*$) and its conversion into flux densities by dividing by the cross sectional area A_{A} ($\mathrm{d}V^*/A_{\text{A}} \to \mathrm{d}\lambda^*$). $j_{\text{B}\to\text{A}}$ is obtained in the same way and it must equal $j_{\text{A}\to\text{B}}$ because of prevailing equilibrium conditions. Because of the proportionalities $\mathrm{e}^{-\beta F(q)} \propto P(q) \propto c(q)$ Eq. 7 reduces to $j_{\text{A}\to\text{B}} = \kappa \cdot \sqrt{\frac{k_{\text{B}}T}{2\pi m}} \cdot \langle c^{\ddagger} \rangle$. Note, furthermore, that our simulations showed that computing TST fluxes, i.e., Eq. 7 and setting $\kappa = 1$, is exactly equivalent to computing one-way fluxes.[13]

We define a critical crystal length for which the tracer transport resistance at the external surface amounts to $\approx$1 percent of the intracrystalline tracer transport resistance by means of the flux densities at the surface and inside the bulk zeolite, respectively,

$$L^{\text{crit}} = 200 \cdot \frac{j^{\text{intra}}}{j^{\text{surf}}/\lambda_{\text{surf}}}. \tag{8}$$

In essence, this length is the minimal crystal dimension in *tracer-exchange experiments* for which the surface transport resistance can, in a good approximation, be neglected in the evaluation model. Note that the factor $200 \triangleq 2 \times 1\%^{-1}$ stems from the consideration of a symmetric plate (compare also Ref. 8).

3 Simulation results

During the MD simulations the core-zeolite loading and the bulk gas-phase concentration were monitored. *Core* and *bulk*, in this context, means that it was sampled inside volumes where effects originating from the crystal surfaces can be certainly neglected (zeolite loading: the $2\times3\times2$ innermost unit cells of the simulation box; gas-phase concentration: volumes at either end of the simulation box with $l_z^{\text{sample}} = 6$ Å). The data from these MD simulations that explicitly include a zeolite *and* a gas space agree very well with adsorption isotherms obtained from Grand-Canonical Monte Carlo (GCMC) simulations in a periodic AFI crystal that were performed with the same potential parameters, see Figure 2. Only in the limit of very large pressures ($p \rightarrow 10^3$ bar), the results are starting to deviate which is due most likely to the formation of a liquid film on the external surface that does affect the bulk gas-phase concentration. The procedure is thus thermodynamcially sound up to several hundred bar. However, it must be pointed out that the potential used is one of the most critical issues in molecular simulation studies. In Figure 2, previously published adsorption isotherms simulated by Maris et al. [38] are plotted for comparison. Although the isotherms found in this work and by Maris et al. are qualitatively similar for ethane, the saturation loadings for ethane differ, and the methane isotherms have even different evolutions. Since their potential was not specifically developed for adsorption in an AFI-type zeolite but Dubbeldam et al. also included an isotherm of methane in $AlPO_4$-5 when determining their potential parameter set,[31] it is believed that the potential used in this work may be considered appropriate. Note that in the following all results are based on MD-NVT simulations, and the GCMC simulations served only as a consistency check.

3.1 Free-energy profiles

In Figure 3, free-energy profiles (left) of single tagged methane (top) and ethane molecules (bottom) in the periphery of the external crystal surface are presented for various total particle numbers inserted into the simulation box. Additionally, the mean potential energy, βU, as experienced by a

single molecule, is plotted right to the F-profiles. At low loadings the free energy in the gas phase is very low but higher than inside the zeolite. This difference is larger for ethane than for methane and it is a consequence of adsorption. The attractive van-der-Waals interaction between adsorbates and adsorbent render the probability to find a molecule inside the zeolite higher than in the gas phase. With increasing loading, θ, and thus pressure, the relative average free-energy level inside the pores increases and, beyond a loading of 5.2 and 4.8 for CH_4 and C_2H_6, respectively, turns to be larger than the free-energy in the gas phase.

Two-dimensional free-energy landscapes, see Figure 4, show that the external surface of both truncations exhibit no holes that might allow the adsorbate molecules to enter previously not accessible zeolite space, i.e., blocked cavities. This would pose a problem to the simple one-dimensional projection of the free-energy landscape. The 1-D free-energy to really enter the zeolite pores would be underestimated in those regions where molecules can be found in both the pore volume and newly accessible cavities. In the worst case it would then change the transition state location, and thus maybe lower the free-energy barrier. Moreover, the 2-D free-energy landscapes confirm the conjecture made in the beginning of the section that a liquid film is forming on the external surface. This is indicated by a second layer condensing onto the external surface (yellow stripe at around -27 Å to -28 Å for θ=9.3 molec./UC). The film forms however at such high pressures that are most likely not relevent to practical applications for the present systems. For this reason, the last 3 state points for methane, compare Figure 2, are not considered anymore in the further analysis. Note that when longer alkanes were to be considered, the liquid film might yet form at pressures that are, in fact, relevant to practical situations. A larger gas-phase volume at the ends of the simulation box would then be neccessary in order to prevent the film of reaching the volumes where the bulk gas-phase concentration is to be sampled and thus of distorting the isotherm.

The F-barrier for entering the zeolite through a window-wise truncated surface is, at low loading, comparable to the intracrystalline barrier for both CH_4 and C_2H_6. As loading increases, the surface barriers to adsorption are getting slightly larger than the intracrystalline barriers. This

phenomenon conversely occurs for the corresponding *desorption* barriers of methane and ethane attempting to leave the zeolite through a window. Here, the surface barriers are larger than the intracrystalline barriers at low loadings, θ, and they are smaller at high θ. Furthermore, as θ increases the transition state (TS) is slightly shifting from a position close to the gas-side basin towards the expected entropic barrier location, i.e., position of the outmost window of the crystal, see Figure 4 as well as Figure 5 in the Supporting Information. As for the cage-wise truncation, these observations are similar, particularly at high loadings. However, the adsorption-desorption barrier difference at low loading is much more pronounced. Also, the TS location remains initially rather constant and then drops sharply at a loading between 3 and 4 molecules per unit cell. The TS locations in the bulk zeolite remain, as expected, stable in all cases. Moreover, the locations of the adsorption and desorption basins remain unchanged over loading, and are identical for both adsorbate types.

The potential-energy profiles in Figure 3 reveal that, additionally to an entropic component, the *intracrystalline* diffusion is also limited by an energetic barrier. As for the surfaces, the steep descent of the potential energy from gas-phase to zeolite crystal indicates very large energetic barriers to the molecules attempting to leave the crystal on either side. Particularly at low loadings, it is energetically very unfavorable to the molecules to leave the crystal in order to stick at the external surface, where they experience the attractive van-der-Waals interaction with the zeolite atoms from one side only. This energetic effect is that strong, that it shifts the TS location from the expected window location more towards the gas phase. Yet, when compared to the free-energy barriers, the βU-desorption barriers are larger. There is thus an entropically more favorable situation at the external surface than in the first zeolite cage. Inside the zeolite, the adsorbates can only move along the *z* direction. Adsorbed on the external surface, the molecules have effectively gained one additional dimension to move (*x* and *y* direction on the external surface, as compared to *z* only inside the pores), which has also been indicated by Arya *et al.*.[12] The entropic gain for methane and ethane are comparable. The energetic drop of ethane is however larger, because C_2H_6 is modelled as 2 beads that, in terms of ε, are comparable to the single methane bead. In any case, the en-

tropic effect becomes more pronounced as loading increases, as evidenced by the larger adsorption barriers at high pressures.

The 2-D free-energy landscapes indicate the general path the molecules take to enter and leave the crystal, respectively. When coming from the zeolite space on the window-wise truncated side of the crystal, they stick in the outmost cage of the crystal and then desorb by creeping around the outer *O*-atoms to eventually reach the external surface. This is evidenced by the yellow region in the outmost cage and the following yellow bended tail (yellow $\triangleq$ high likelihood to find the molecule). As for the cage-wise truncated side, this process is similar. However, the creeping-around is less evident at low loadings. This is, because the end regions comprise of open pore cages providing less external surface to stick on such that the molecules are partially on the external surface but also in the half end cage. Elevating the pressure results finally again in a distinct "creeping path". In the bulk zeolite, the molecules also take a hopping path that is located close to the pore walls, see Figure 4 in the Supporting Information.

Note finally that the free-energy and the potential-energy profiles of methane at very low loadings agree well with potential of mean force and average potential-energy profiles published by Arya *et al.*[12]

3.2 Transmission coefficient

Reactive flux correlation functions (RFCFs) of methane in a periodic AFI crystal and at the crystal ends are shown in Figure 5 and Figure 6. The overall RFCF is comprised of two contributions:

1. Those trajectories that start with a velocity of the tagged molecule on the barrier that points toward the target cage/free-energy basin, $\kappa^{+}(t)$.

2. Those that start with a reverse velocity, $\kappa^{-}(t)$.

The overall RFCF is the sum of the 2 contributions, i.e., $\kappa(t) = \kappa^{+}(t) + \kappa^{-}(t)$, see also Ref. 39.

In the case of a periodic crystal, the overall RFCF decays exponentially with time, as do the two separate contributions (Figure 5). The decay time, t^{decay}, for a given loading, is thereby the

same for all three functions. Furthermore, t^{decay} increases with loading, giving rise to retardation of the barrier crossing because of the interaction between the tagged molecule and surrounding molecules. Interestingly, the plateau value of both the positive and negative contribution decrease almost equally in magnitude when loading increases.

The situation is quite different at the crystal surface. There are two to three time frames observable for the decay of the RFCFs. A short decay time, that is comparable to the intracrystalline t^{decay}, occurs always for the positive contribution of those tagged molecules that aim to enter the zeolite ($\kappa^{+}_{\mathrm{ads}}$), and the negative contribution of those trying to desorb. A long decay time occurs for the other two cases (positive contribution to desorb, and negative contribution to adsorb, respectively). Additionally to these 2 time frames, there is a third decay time, that is observable for $\kappa^{+}_{\mathrm{ads}}$ and $\kappa^{-}_{\mathrm{des}}$ at the cage-wise truncated crystal side and low loadings only, see Figure 6. In those cases, there are 2 plateaus for $\kappa^{+}_{\mathrm{ads}}$ and $\kappa^{-}_{\mathrm{des}}$. Irrespective of the different decay mechanisms, the overall RFCFs of adsorption and desorption are identical for a given crystal side and loading.

The different decay times have their origin most likely in the asymmetry of the barriers and the different length scales for reaching state A and B, respectively. Evidence to this is provided by time-resolved phase-space plots of the entire swarm of RFCF shoots from the barrier, see Figure 7 (CH_4 at the cage-wise truncated surface at a loading of 0.88 molec./UC). Each plot is a "snapshot" that represents the probability of finding the tagged molecule, after some time t, at some point in q, when it had initially a velocity of $\dot{q}(0)$. The first plot at non-zero time (0.1 ps) shows the typical evolution of the diagrams when the barriers are symmetric and the crossing process non-diffusive (for example, intracrystalline barrier crossings of methane in AFI). The sequences, in those cases, indicate ballistic motion, i.e., $q(t) = \dot{q}(0) \cdot t$, such that the entire distribution sequence appears as a clockwise rotation around [$q = 0$, $\dot{q}(0) = 0$] up to the point where the trajectories reach their initially aimed state. In the present case, however, the trajectories evolve differently (Figure 7, t =0.4 ps):

1. The first trajectories with initially positive velocities, i.e., that aimed to desorb, have reached the crystal surface whereas all those trajectories that aimed to adsorb are yet "under way"

because of the different length scales of the adsorption and desorption states, as measured from the barrier.

2. The center of the "distribution pendulum" (red strip) has shifted such that a much larger fraction of the desorbing-aiming trajectories has been sucked into the zeolite than the initially adsorbing-aiming having redirect towards the crystal surface. This is probably because of the attractive van-der-Waals potential.

3. The large area of yellow color indicates a very broad distribution. Since 0.4 ps is a rather short time to observe this "smearing" of the distribution, it can be concluded that the barrier crossing at the surface is quite diffusive.[40]

From the following plots, t >0.4 ps, it can be seen that the desorption state is "filled up" quite continously over time with trajectories for which $\dot{q}(0)$ >0 which confirms that $\kappa^{+}_{\mathrm{des}}(t)$ decays continuously. The negative contribution to the desorption attemps exhibits a plateau between 0.4 and 0.8 ps which may be due to the fact that some molecules attempted to adsorb (negative $\dot{q}(0)$), hit on the concluding half cage of the crystal such to be immediately reflected and quickly reach the desorbing state, as evidenced by the slight yellow strip for $q > 0$, $\dot{q}(0) < 0$, t =0.4, and 0.8 ps. The time for this plateau to be reached (0.4 ps) supports this conjecture, because the mean travelled distance based on this time and an average absolute velocity in z-direction of 3.15 $\mathrm{\AA/ps}$ from kinetic gas theory yields a value (1.3 Å) that is similar to the distance of the desorption state from the barrier (1.85 Å). Between 0.4 and 0.8 ps, none of the remaining adsorption-aiming trajectories have been reflected but they are smoothly sucked in by the attractive zeolite potential. Also, the first trajectories, mostly with high initial momentum (< -500 m/s), have reached the adsorption state within this time. In the time between 0.8 and 2.5 ps there is again a considerable fraction of trajectories recrossing that initially aimed to adsorb. The intermediate plateau and the subsequent long second decay time of $\kappa^{-}_{\mathrm{des}}(t)$ come thus from the somewhat lengthy way of the molecules into the interior of the crystal where they reside for some time, and then partially travel back toward the surface.

The transmission coefficients, κ, are identified as the plateau values of the overall RFCFs. They are displayed in Figure 8 as functions of core-zeolite loading. As for the intracrystalline case, the transmission coefficients of both adsorbates are very similar. Starting from around unity at infinite dilution, the transmission coefficient decreases only slightly, but, for loadings beyond 1 molecule per unit cell, it decreases almost linearly. There is however a somewhat sharp drop at $\theta = 4$ for ethane such that it rather remains constant at subsequent loadings. As a consistency check, correlation factors on basis of mean first-passage times[41] were computed for methane in a periodic AFI crystal at three loadings (θ =0, 2, and 4 molecules per unit cell; asterisks in Figure 8). The correlation factors, f^{fp}, on basis of mean first-passage times, $\overline{t}^{\mathrm{fp}}$, were computed by following equation

$$f^{\mathrm{fp}} = \frac{0.5}{\overline{t}^{\mathrm{fp}} \cdot k^{\mathrm{TST}}_{\mathrm{A}\rightarrow\mathrm{B}}} \tag{9}$$

where $k^{\mathrm{TST}}_{\mathrm{A}\rightarrow\mathrm{B}}$ is the TST hopping frequency, as computed from free-energy profiles. Note that the factor 0.5 in Eq. 9 stems from considering a one-dimensional lattice where a molecule that starts from a given lattice site, say A, may hop to either the left, B*, or right, B, neighboring lattice site with each 50% probability. The RFCF method and the first-passage time approach yield the same values.

The transmission coefficients at the surfaces behave quite differently. They neither start from around unity, nor do they depend much on loading. However, recrossing is a symmetric phenomenon, i.e., $\kappa^{\mathrm{ads}} = \kappa^{\mathrm{des}}$ for a given loading at one and the same surface. Although the data scatter, a trend is observable for methane at the window-wise truncated side: linearly decreasing from 0.63 ($\theta = 0.3$) to 0.43 ($\theta = 4$), afterwards constant. As for the cage-wise truncation, a similar trend is observable, here from 0.53 to 0.33. Interestingly, κ seems to be constant for ethane at low loadings, yielding for both truncations a value of around 0.45. Beyond 4 molecules per unit cell, the transmission coefficient drops sharply and increases then again. This together with additional correlation plots that are found in the Supporting Information further supports the earlier statement of much more diffusive barrier crossing at the crystal surface, as compared to intracrystalline barrier crossing.

3.3 Permeability and critical crystal length

On basis of the free-energy barriers and the RFCF data, surface permeabilities have been computed, see Figure 9, where α_S is plotted as a function of loading for methane (top) and ethane (bottom) and both crystal truncations (window-wise $\leftrightarrow$ cage-wise). Since the transmission coefficients of ethane were only computed at 4 state points, interpolation/extrapolation was neccessary:

- Window truncation: κ=0.45 for $\theta \leq$3.2 molec./UC; κ=0.3 otherwise.
- Cage truncation: κ=0.45 for $\theta \leq$3.2 molec./UC; κ=0.25 otherwise.

Because, on the one hand, the adsorption and desorption barriers for a given fluid and crystal side are generally not equal but, on the other hand, the transmission coefficients are equal, it is observed that $\alpha_S^{ads} \neq \alpha_S^{des}$. The adsorption permeability is, at low loadings, always larger than the corresponding desorption permeability. The difference between permeabilities obtained at the cage-wise truncated crystal surface are thereby always larger than those obtained at the window truncation. The further trends of the surface permeabilities as functions of loading reflect the trends of the free-energy barriers with loading. This is, α_S^{ads} decreases with loading, because the corresponding barrier increases. As for desorption, this holds the other way around. This leads eventually to an intersection of α_S^{ads} and α_S^{des} at intermediate loadings which marks the point of equal hopping rates for adsorption and desorption.

In Figure 10, the critical crystal length, L^{crit}, is plotted as a function of the unit-cell loading. Since the adsorption and desorption fluxes are equal for one and the same crystal truncation (compare Section 2.3.1), Eq. 8 yields the same critical crystal length for adsorption and desorption at a given crystal side. The influence of the way the external surface was realized (window trunction $\leftrightarrow$ cage truncation) has hardly an influence which confirms earlier findings.[12] Over the loading regimes studied, L^{crit} decreases from around 1000 nm, and 5000 nm, for CH_4 and C_2H_6 respectively, to 100 nm. Hence the critical crystal length is in the range of producible zeolite crystal sizes ($> 1\mu$m) solely for ethane at low loadings/pressure, and can consequently be neglected for methane. Diminishing surface barriers with increasing loading and pressures, respectively, were also

observed by Arya *et al.*[12] for methane diffusing through an $AlPO_4$-5 crystal, and by Newsome and Sholl[13,14] for methane, ethane, and tetrafluoromethane through a silicalite crystal.

The instance that the actual external surface has no large impact on L^{crit} suggests that the surface transport resistance is merely dependent on a quantity that is not connected to crystal properties. It turns out that it is the average one-dimensional gas-phase flux in z toward the crystal

$$j^{\mathrm{gas}} = \langle c^{\mathrm{gas}} \rangle \cdot \langle v^{\mathrm{gas}}_{z,+} \rangle = \langle c^{\mathrm{gas}} \rangle \cdot \sqrt{\frac{k_{\mathrm{B}} T}{2\pi m}}. \tag{10}$$

Substituting j^{surf} with j^{gas} in Eq. 8, and furthermore, for simplicity, setting $\lambda_{\mathrm{surf}} = \lambda_{\mathrm{intra}}$ and neglecting the dynamical correction for j^{intra} leads finally to

$$L^{\mathrm{crit}} = 200 \cdot \frac{\langle c^{\mathrm{zeol}} \rangle}{\langle c^{\mathrm{gas}} \rangle} \cdot \frac{\mathrm{e}^{-\beta F(q^{\ddagger})}}{\int\limits_{\text{cage A}} \mathrm{e}^{-\beta F(q)} \cdot \mathrm{d}q} \cdot \lambda^2_{\mathrm{intra}}. \tag{11}$$

This small model equation that is merely based on rapidly accessible data from molecular simulation – effectively, an adsorption isotherm for $\langle c^{\mathrm{zeol}} \rangle / \langle c^{\mathrm{gas}} \rangle$, and histograms for the relative probability to find the molecule inside the periodic crystal on top of the barrier – gives, at least on the order of magnitude, a reliable estimate for the critical crystal length at low to intermediate loadings (dashed lines in Figure 10). Both input data to the model could be harvested in one and the same *periodic-crystal* GCMC simulation. Interestingly, the match is much better for ethane than for methane. However, the trend is, up to intermediate loadings of around 4 to 5 molecules per unit cell, always correct. At high pressures, large deviations between the model and the simulation data are observed. This can nor be governed by a fugacity-wise corrected concentration for computing the gas-phase flux which would account for non-idealities (solid lines in Figure 10).

4 Conclusions

As compared with detailed molecular modeling, a thermodynamic model that has been derived within this work captures the main features of the influence of the surface effects when those are of

significance. Some deviation were yet observed – particularly at high pressures. From a different point of view, the departure of the model from the simulation results marks the point at which the external surface itself has an influence on the surface effects, because the model is mainly based upon gas-phase properties. Even more intriguing is the extrapolation to additional chemical barriers, i.e., when, for example, silanol groups are introduced in order to saturate the external surface. Such groups will certainly decrease the surface transport,[22] and, hence, increase the critical crystal length. The overall surface transport is thus controlled by gas-phase effects ($L^{\mathrm{crit}}_{\mathrm{gas}}$), structural factors resulting from chemically highly idealized surfaces ($L^{\mathrm{crit}}_{\mathrm{surface}} = L^{\mathrm{crit}}_{\mathrm{windows}}, L^{\mathrm{crit}}_{\mathrm{cages}}$), and a chemical component due to silanol groups and the like ($L^{\mathrm{crit}}_{\mathrm{silanol}}$). The pure impact of the latter two could then be quantified by $(L^{\mathrm{crit}}_{\mathrm{surface}} - L^{\mathrm{crit}}_{\mathrm{gas}})/L^{\mathrm{crit}}_{\mathrm{gas}}$ and $(L^{\mathrm{crit}}_{\mathrm{silanol}} - L^{\mathrm{crit}}_{\mathrm{surface}})/L^{\mathrm{crit}}_{\mathrm{surface}}$, see also Figure 11. The chemical barriers were deduced from the work of Thompho *et al.*[22] who have computed adsorption permeabilities for methane in MFI with and without saturating the external surface with silanol. The permeabilities decreased by a factor of 5 when silanol was introduced so that j^{surf} was decreased by the same factor for computing $L^{\mathrm{crit}}_{\mathrm{silanol}}$ in Figure 11, and $(L^{\mathrm{crit}}_{\mathrm{silanol}} - L^{\mathrm{crit}}_{\mathrm{surface}})/L^{\mathrm{crit}}_{\mathrm{surface}}$ is hence approximately 4.

This view on the different retarding effects may possibly be used for tayloring the external surface such that it fits the design purposes of adsorbers and heterogenous reactors. Imagine, for example, a multicomponent stream within a given chemical process line. At a certain point, the stream comprises 2 components both of which may enter the micropores of a given zeolite crystal rather facile on a size basis. Because of different chemical properties, however, the surface can be tuned such that it forms chemical barriers to one component that is unwanted in the interior of the micropores. In the context of molecular path control[42] which may be seen as a "degree of freedom to membrane design purposes", the surface tayloring described above provides a new and independent "design degree of freedom".

Another interesting conclusion can be drawn with respect to the transferability of the results of equilibrium permeation to gradient-driven permeation. Since the transport coefficients of self diffusion and collective diffusion become very similar at very low pressures ($\rightarrow$ infinite dilution),

and as the results of this work indicate that surface effects are, for the present cases, important only at low loadings/pressures, the critical crystal lengths computed will approximately also be valid in the case of gradient-driven permeation. Newsome and Sholl[13,14] have thereby provided evidence to this conjecture, and have proposed a method that uses equilibrium one-way fluxes and transport diffusivities in order to assess critical crystal lengths for variable driving forces. So, for a quick estimation of the influence of surface effects on basis of at least the simplest possible factor – the gas-phase flux – one merely needs to compute an adsorption isotherm with simultaneous computation of histogram data inside the *periodic* crystal. By means of reweighting methods, e.g. as proposed by Schüring et al.,[43] and with the aid of the method introduced by Newsome and Sholl,[13,14] the influence of surface effects can be rapidly estimated at various state points (T) and for various driving force (Δp).

Ultimately, we have, from a technological point of view, assessed transport resistances of technically relevant adsorbates, and, owing to the detailed analysis of the molecular simulation performed, pictorial insights into the permeation processes have been achieved. From a scientific point of view, we have rigorously expanded the use of extended dynamically corrected transition state theory from intracrystalline diffusion to equilibrium permeation of tracers into and out of zeolite crystals.

Acknowledgement

NERZ would like to thank Prof. Dr. S. Vasenkov for stimulating comments during the Annual AIChE conference (2008 in Philadelphia), and Dr. S. Fritzsche for helpful discussions and critical reading of the manuscript. Also, we would like to thank the reviewers who have, by means of their expert comments and criticism, enhanced the quality of this article. This work was supported by the Deutsche Forschungsgemeinschaft (DFG, priority program SPP 1155).

Supporting Information Available

This material includes a discussion of the thermostat used in this work – the ”Lowe-Andersen ther-

mostat for interface-fluid collisions", and a detailed description of dynamically corrected transition state theory. Moreover, the shifting of the transition states of molecules adsorbing and desorbing into and out of the crystal is discussed, together with 2-dimensional free-energy profiles of adsorbates in the bulk crystal. Finally, the concept of a committor probability, and the use of correlation plots of the RFCF are being explained and discussed. This material is available free of charge via the Internet at http://pubs.acs.org.

References

(1) Davis, M. E. *Nature* **2002**, *417*, 813–821.

(2) Wheatley, P. S.; Butler, A. R.; Crane, M. S.; Fox, S.; Xiao, B.; Rossi, A. G.; Megson, I. L.; Morris, R. E. *J. Am. Chem. Soc.* **2006**, *128*, 502–509.

(3) Beerdsen, E.; Smit, B.; Dubbeldam, D. *Phys. Rev. Lett.* **2004**, *93*, 248301.

(4) Dubbeldam, D.; Beerdsen, E.; Vlugt, T. J. H.; Smit, B. *J. Chem. Phys.* **2005**, *112*, 224712.

(5) Krishna, C. A.; Yoshanath, S.; Schüring, A.; Kärger, J.; Fritzsche, S. *J. Chem. Phys.* **2009**, *submitted*.

(6) Kärger, J.; Ruthven, D. M. *Diffusion in Zeolites and Other Microporous Solids*; John Wiley & Sons Inc.: New York, 1992.

(7) Schemmert, U.; Kärger, J.; Weitkamp, J. *Micropor. Mesopor. Mater.* **1999**, *32*, 101–110.

(8) Heinke, L.; Kortunov, P.; Tzoulaki, D.; Kärger, J. *Phys. Rev. Lett.* **2007**, *99*, 228301.

(9) Webb, E. B.; Grest, G. S. *J. Chem. Phys.* **2002**, *116*, 6311–6321.

(10) Schüring, A.; Vasenkov, S.; Fritzsche, S. *J. Phys. Chem. B* **2005**, *109*, 16711–16717.

(11) Gulín-González, J.; Schüring, A.; Fritzsche, S.; Kärger, J.; Vasenkov, S. *Chem. Phys. Lett.* **2006**, *430*, 60–66.

(12) Arya, G.; Maginn, E. J.; Chang, H.-C. *J. Phys. Chem. B* **2001**, *105*, 2725–2735.

(13) Newsome, D. A.; Sholl, D. S. *J. Phys. Chem. B* **2005**, *109*, 7237–7244.

(14) Newsome, D. A.; Sholl, D. S. *Micropor. Mesopor. Mater.* **2008**, *107*, 286–295.

(15) Ahunbay, M. G.; Elliott, J. R.; Talu, O. *J. Phys. Chem. B* **2002**, *106*, 5163–5168.

(16) Arya, G.; Chang, H.-C.; Maginn, E. J. *J. Chem. Phys.* **2001**, *115*, 8112–8124.

(17) June, R. L.; Bell, A. T.; Theodorou, D. N. *J. Phys. Chem.* **1991**, *95*, 8866–8878.

(18) Qiu, S.; Pang, W.; Kessler, H.; Guth, J. L. *Zeolites* **1989**, *9*, 440–444.

(19) Lin, Y. S.; Kumakiri, I.; Nair, B. N.; Alsyouri, H. *Separat. Purific. Meth.* **2002**, *31*, 229–379.

(20) Kanezashi, M.; Lin, Y. S. *J. Phys. Chem. C* **2009**, *113*, 3767–3774.

(21) Caro, J.; Noack, M. *Micropor. Mesopor. Mater.* **2008**, *115*, 215–233.

(22) Thompho, S.; Chanajaree, R.; Remsungnen, T.; Hannongbua, S.; Bopp, P. A.; Fritzsche, S. *J. Phys. Chem. A* **2009**, *113*, 2004–2014.

(23) Terasaki, O. *J. Electron Microsc.* **1994**, *43*, 337–346.

(24) Lehmann, E.; Chmelik, C.; Scheidt, H.; Vasenkov, S.; Staudte, B.; Kärger, J.; Kremer, F.; Zadrozna, G.; Kornatowski, J. *J. Am. Chem. Soc.* **2002**, *124*, 8690–8692.

(25) Zimmermann, N. E. R.; Jakobtorweihen, S.; Beerdsen, E.; Smit, B.; Keil, F. J. *J. Phys. Chem. C* **2007**, *111*, 17370–17381.

(26) Jakobtorweihen, S.; Verbeek, M. G.; Lowe, C. P.; Keil, F. J.; Smit, B. *Phys. Rev. Lett.* **2005**, *95*, 044501.

(27) Jakobtorweihen, S.; Lowe, C. P.; Keil, F. J.; Smit, B. *J. Chem. Phys.* **2006**, *124*, 154706.

(28) Jakobtorweihen, S.; Keil, F. J.; Smit, B. *J. Phys. Chem. B* **2006**, *110*, 16332–16336.

(29) Martyna, G. J.; Tuckerman, M. E.; Tobias, D. J.; Klein, M. L. *Mol. Phys.* **1996**, *87*, 1117–1157.

(30) Dubbeldam, D.; Calero, S.; Vlugt, T. J. H.; Krishna, R.; Maesen, T. L. M.; Beerdsen, E.; Smit, B. *Phys. Rev. Lett.* **2004**, *93*, 088302.

(31) Dubbeldam, D.; Calero, S.; Vlugt, T. J. H.; Krishna, R.; Maesen, T. L. M.; Smit, B. *J. Phys. Chem. B* **2004**, *108*, 12301–12313.

(32) Beerdsen, E.; Smit, B. *J. Phys. Chem. B* **2006**, *110*, 14529–14530.

(33) Bennett, C. H. *Thin Solid Films* **1975**, *25*, 65–70.

(34) Chandler, D. *J. Chem. Phys.* **1978**, *68*, 2959–2970.

(35) Radhakrishnan, R.; Schlick, T. *J. Chem. Phys.* **2004**, *121*, 2436–2444.

(36) Peters, B.; Zimmermann, N. E. R.; Beckham, G. T.; Tester, J. W.; Trout, B. L. *J. Am. Chem. Soc.* **2008**, *130*, 17342–17350.

(37) Schüring, A. *J. Phys. Chem. C* **2007**, *111*, 11285–11290.

(38) Maris, T.; Vlugt, T. J. H.; Smit, B. *J. Phys. Chem. B* **1998**, *102*, 7183–7189.

(39) Kuharski, R. A.; Chandler, D.; J. A. Montgomery, J.; Rabii, F.; Singer, S. J. *J. Phys. Chem.* **1988**, *92*, 3261–3267.

(40) Frenkel, D.; Smit, B. *Understanding Molecular Simulations, From Algorithms to Applications*; Academic Press: San Diego, 2002.

(41) Helfand, E. *J. Chem. Phys.* **1978**, *69*, 1010–1018.

(42) Dubbeldam, D.; Beerdsen, E.; Smit, B. *Proc. Nat. Acad. Sci.* **2005**, *102*, 12317–12320.

(43) Schüring, A.; Auerbach, S. M.; Fritzsche, S. *Chem. Phys. Lett.* **2007**, *450*, 164–169.

Table 1: Potential Parameters. The Lennard–Jones (L–J) interactions are only for non-bonded pairs.

Type	σ, r_0 [Å]	ε/k_B, k^{bond}/k_B [K], [K/Å^2]
L–J CH_4–CH_4	3.72	158.5
L–J CH_4–O	3.47	115.0
L–J CH_3–CH_3	3.76	108.0
L–J CH_3–O	3.48	93.0
harmonic bond CH_3–CH_3	1.54	96500.0

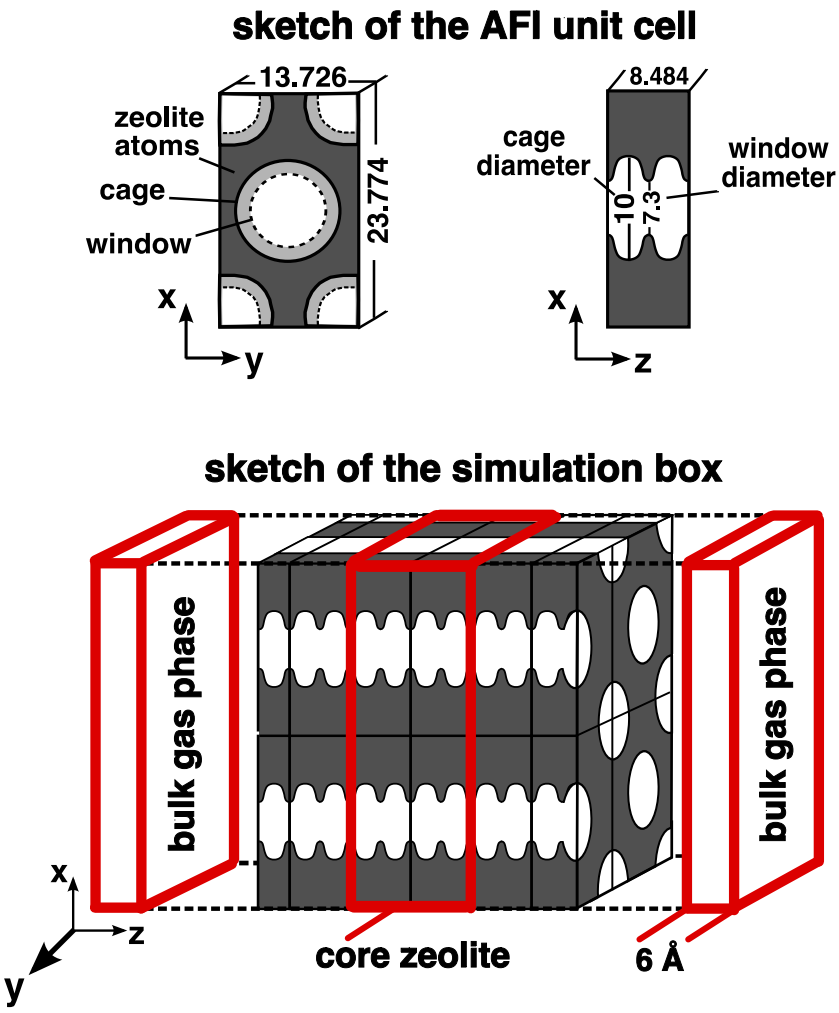

Figure 1: Top: sketch of the AFI unit cell - two different projections. Dark grey areas correspond to areas/volumes occupied by zeolite atoms being thus inaccessible for adsorbate molecules of the size of a methane molecule or larger. White areas indicate accessible volumes to adsorbates and light grey rings in the *x*-*y*-projection indicate the varying pore diameter along *z*. Note that the original monoclinic structure was converted to an orthorhombic unit cell. Bottom: simulation box (cut along *x*-*z* plane at y=0 Å). 10 entire cages are accomodated in each pore of the crystal. The windows of the AFI structure form the entrance to molecules coming from the left-hand gas phase ($z < 0$); the cages conclude the crystal on the right-hand side ($z > 0$). The thick (red) lines indicate the volumes of *bulk* gas phase and *core* zeolite, i.e., where the gas concentration and the zeolite loading were sampled.

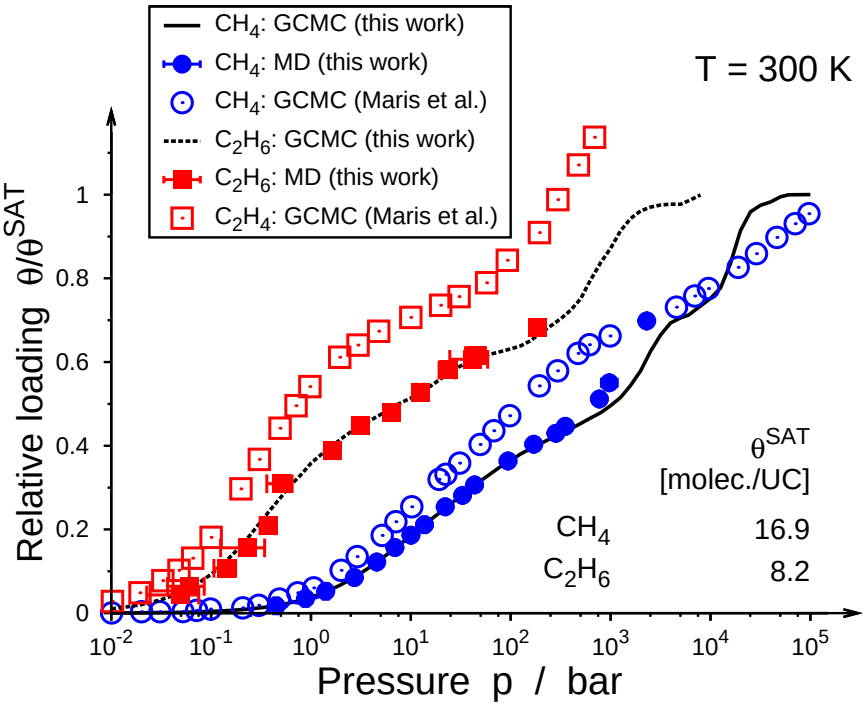

Figure 2: Adsorption isotherms for methane and ethane in an all-silica AFI-type zeolite at 300 K. The lines are results obtained from conventional Grand-Canonical Monte Carlo simulations in a periodic AFI crystal; the filled squares and filled circles are results from MD simulations where a gas phase is brought into contact with a thin AFI crystal. In the case of MD simulations, the gas pressure was estimated using the gas-phase concentration and the Peng-Robinson equation of state; in case of GCMC simulations, the same equation of state was used in order to compute the fugacity. The open symbols are results from Maris et al. who used a different force field.[38]

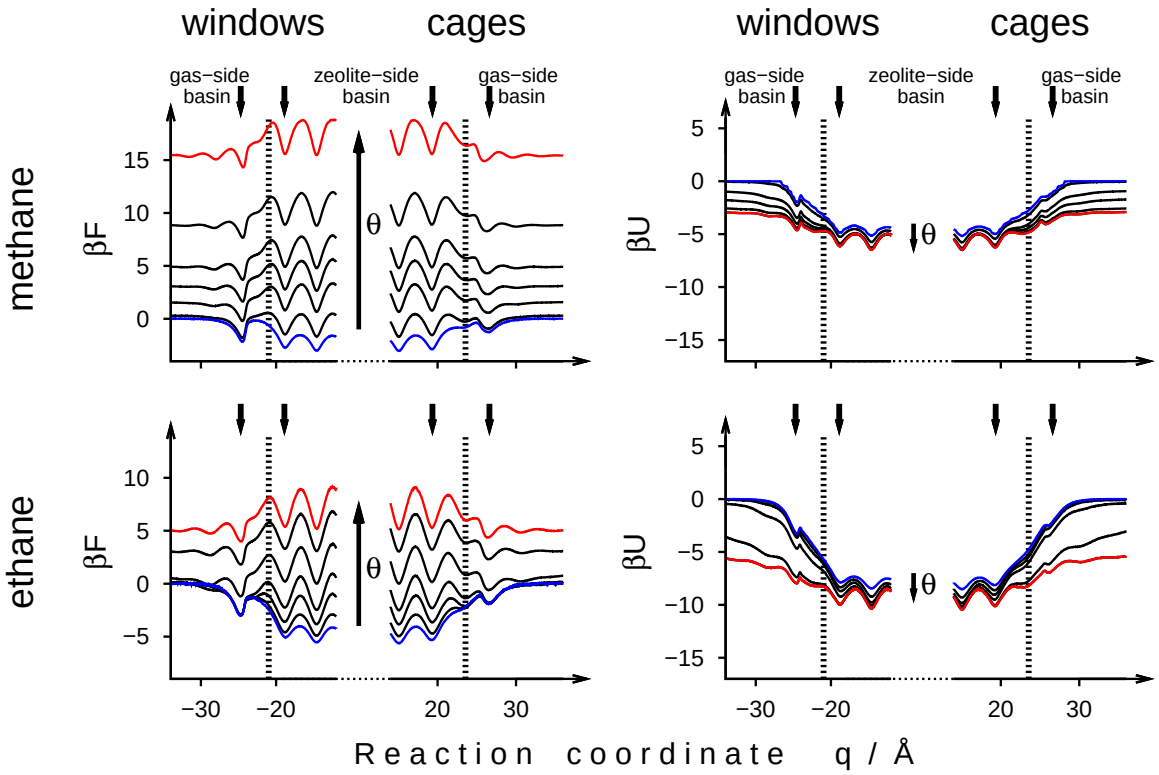

Figure 3: Normalized free energy, $\beta F = F/(k_{\mathrm{B}}T)$ (left), and mean potential energy of a single tagged molecule, βU (right), as functions of reaction coordinate, q, displayed for the end regions of the crystal. The center of the simulation box is located at $q = z = 0$. The thick dotted lines indicate the positions of the outmost *O*-atoms on either side of the crystal (window-wise and cage-wise truncation). The profiles were computed for methane (top) and ethane (bottom) in an all-silica AFI crystal at 300 K and various total molecule numbers, N^{part}. The resulting average loadings, θ, were 0.6, 4.3, 6.1, 6.8, 7.3, 7.6, as well as 9.3 molecules per unit cell and 0.5, 2.5, 3.7, 4.3, 4.97, 5.05, as well as 5.6 molecules per unit cell for methane and ethane, respectively.

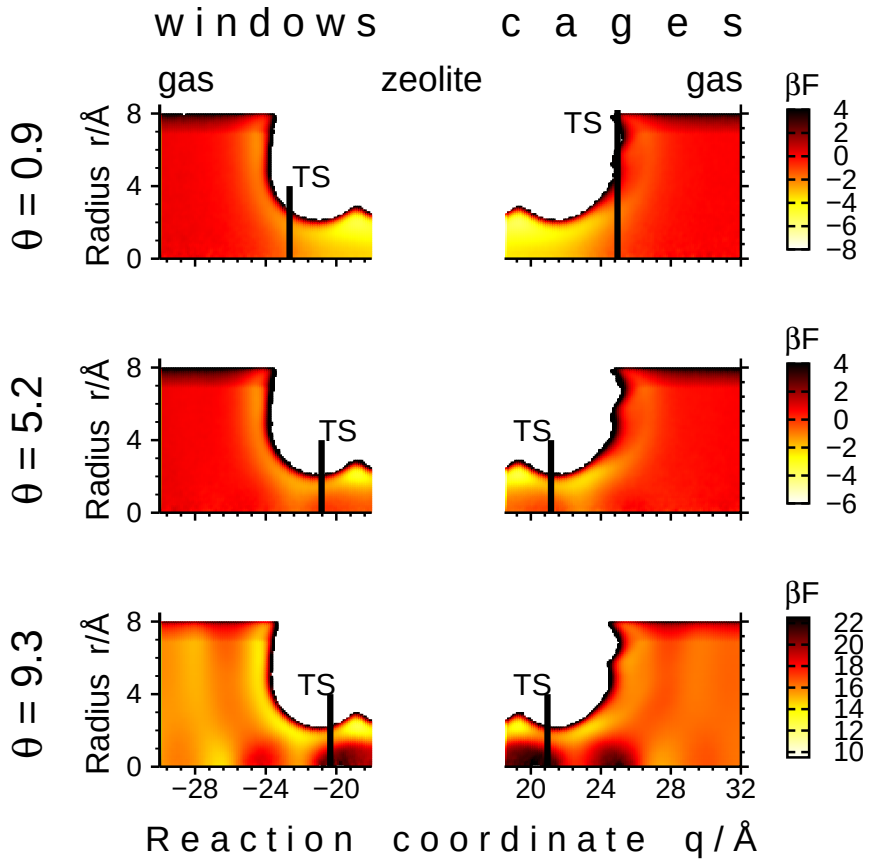

Figure 4: Free-energy landscape, βF, projected onto the plane of the reaction coordinate, q, and the radius from the pore center, r, around the pore mouth of the crystal (CH_4 in all-silica AFI-type crystal at 300 K). Top down: loading, θ, increases from 0.9, over 5.2, to 9.3 molecules per unit cell. Left: window-wise truncation of the crystal; right: cage-wise truncation. Note that the lower βF at 6.5 Å $\leq r \leq$8 Å are caused by the diminishing sampling volumes because the radii of adjacent pores start to overlap. Dark areas indicate regions where it is rather unlikely to find the tagged molecule whereas yellow represents areas where the molecule is very likely to be found. The colorbox range is chosen such that white areas were never visited by a molecule. The location of the respective transition state/bottleneck (TS) is indicated by a thick vertical line in each plot.

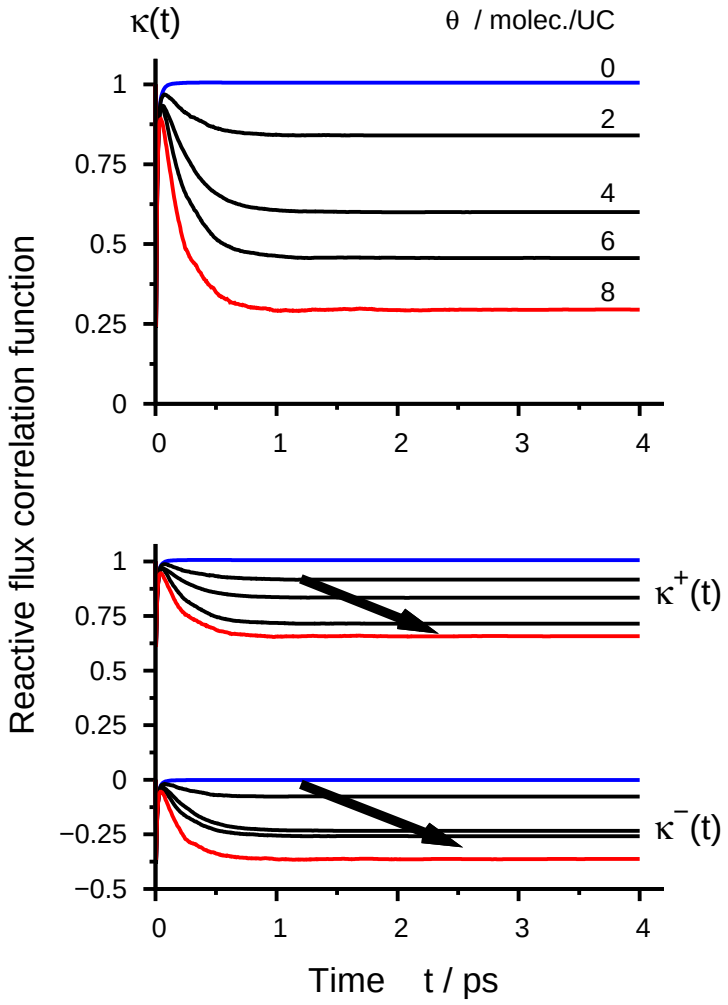

Figure 5: Overall reactive flux correlation function, $\kappa(t)$ (top), as well as its positive, $\kappa^{+}(t)$, and negative contribution, $\kappa^{-}(t)$ (the latter two: bottom), for methane in a periodic AFI crystal at 300 K and various loadings: zero loading (0 molec./UC), 2, 4, 6, and 8 molecules per unit cell. Arrows (bottom) indicate the change of $\kappa^{+}(t)$ and $\kappa^{-}(t)$ with increasing loading.

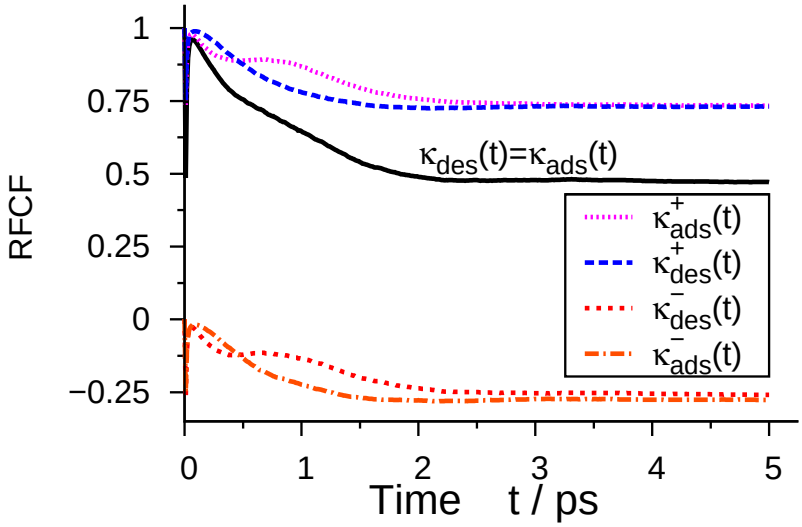

Figure 6: Overall reactive flux correlation function (RFCF), $\kappa(t) = \kappa_{\mathrm{des}}(t) = \kappa_{\mathrm{ads}}(t)$, as well as the respective positive, $\kappa^{+}_{\mathrm{des/ads}}(t)$, and negative contribution, $\kappa^{-}_{\mathrm{des/ads}}(t)$, for methane attempting to leave (subscript des) and enter (ads) the AFI crystal at the cage-wise truncated surface at an average loading of 0.6 molecules per unit cell (300 K).

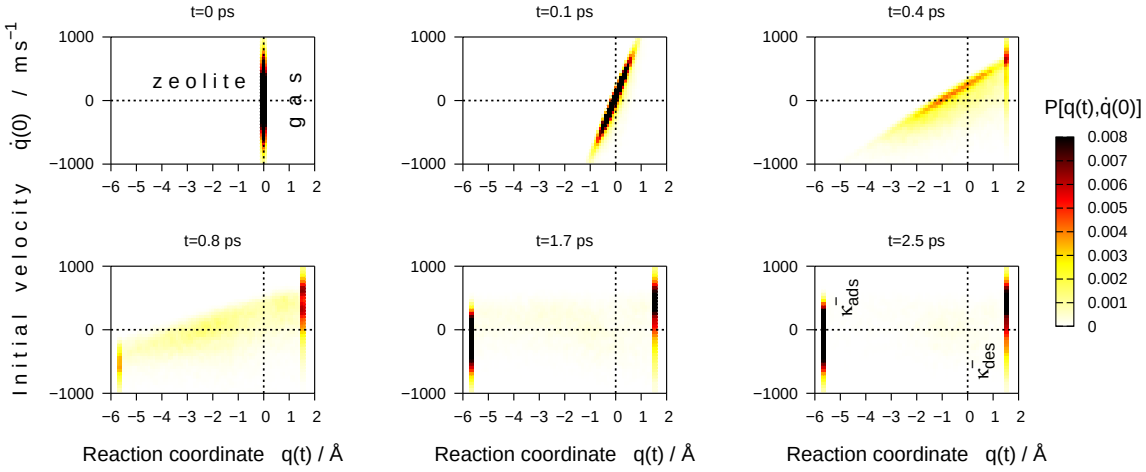

Figure 7: Time resolved phase-space plots, $P[q(t), \dot{q}(0)]$, of trajectories starting from the adsorption/desorption barrier; methane at the cage-wise truncated crystal surface (300 K, θ=0.88 molec./UC). Note that q was shifted such to find the transition state at $q = 0$.

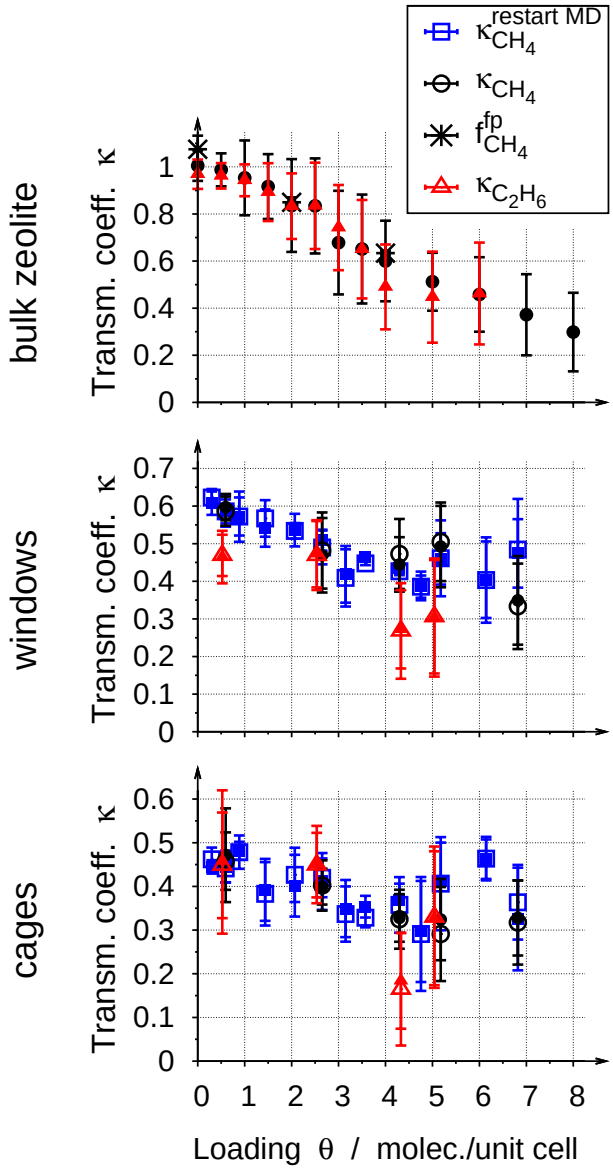

Figure 8: Transmission coefficient, κ, as a function of loading, θ, for methane and ethane (AFI crystal, 300 K). Top: inside a periodic crystal (bulk zeolite); center: surface with window-wise truncation; bottom: surface with cage-wise truncation. As for the surface cases, two κs were computed for one and the same state point and truncation plane: the small filled symbols correspond to the transmission coefficients for the zeolite-side (desorption), and the larger open symbols to κs found for the gas-side process (adsorption). The two values agree very well with one another. The circles and triangles refer to RFCF simulation results in which an entirely new initial configuration was computed as starting point for the EPS starting-configuration sampling; the squares refer to simulation results where the initial configuration for EPS was taken from the final MD configuration of the histogram sampling. The asterisks are correlation factors that are based on TST hopping rates, $k^{\mathrm{TST}}_{A\to B}$, and mean first-passage times, $\overline{t}^{\mathrm{fp}}$ (bulk zeolite only: $\theta = 0$, 2, and 4 molec./unit cell).

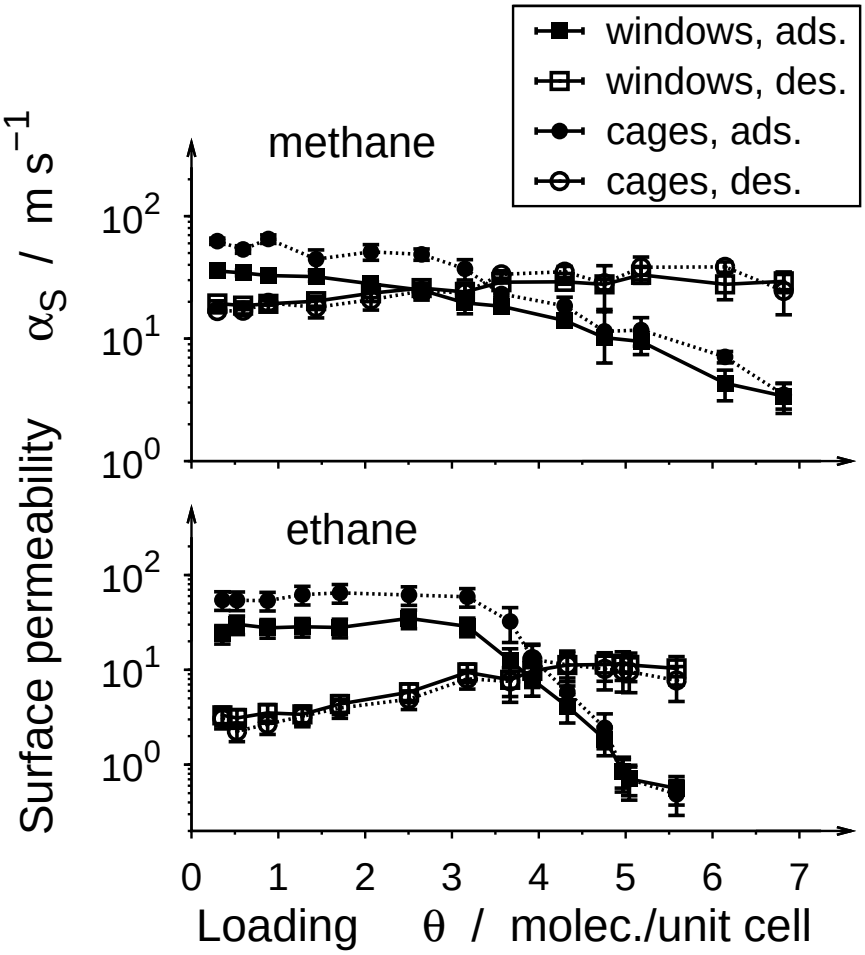

Figure 9: Equilibrium surface permeability, α_S, as a function of zeolite loading, θ, for methane (top) and ethane (bottom) and both truncation realizations (window truncation: squares, cage: circles). The open symbols correspond to desorption permeabilities; the filled ones thus to the adsorption α_Ss. The errors are estimated by error propagation of the transmission coefficient, κ, because they constitute the largest error source. The lines shall guide the eye.

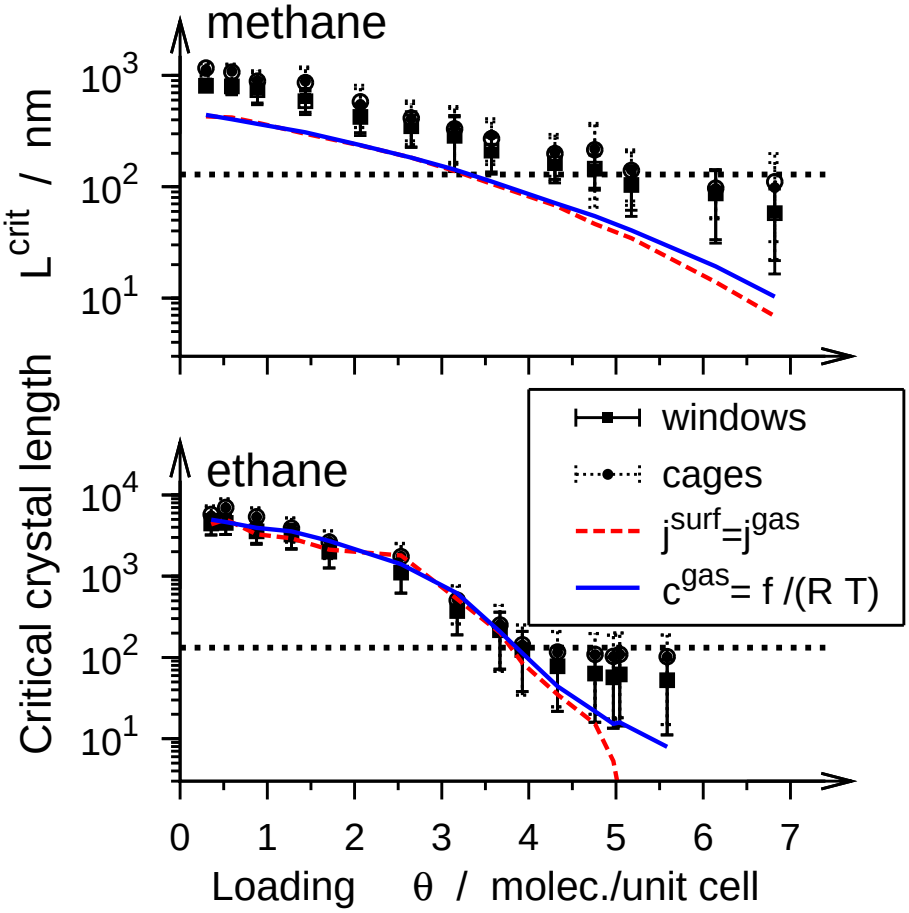

Figure 10: Critical crystal length, L^{crit}, as a function of core-zeolite loading, θ, for methane (top) and ethane (bottom). The small filled symbols are results deduced from adsorption fluxes; the large open symbols were obtained from the corresponding desorption fluxes. For one and the same condition and crystal truncation, $L^{\text{crit}}_{\text{ads}}$ and $L^{\text{crit}}_{\text{des}}$ are equal for which reason the corresponding open and filled squares (window truncation) and circles (cage truncation) appear as one large filled symbol. The dashed lines are estimates based upon rapidly assessable quantities ($j^{\text{surf}} = j^{\text{gas}}$, $\lambda_{\text{surf}} = \lambda_{\text{intra}}$, $j^{\text{intra}} = \lambda_{\text{intra}} k^{\text{TST}}_{\text{intra}} \bar{c}_{\text{zeol}}$), and the solid lines incorporate a small improvement to the simple model that accounts for nonidealities of the fluid (fugacity-wise corrected gas-phase concentration, $c^{\text{gas}} = f/[RT]$). The dotted horizontal lines mark the situations when $j^{\text{surf}} = j^{\text{intra}}$.

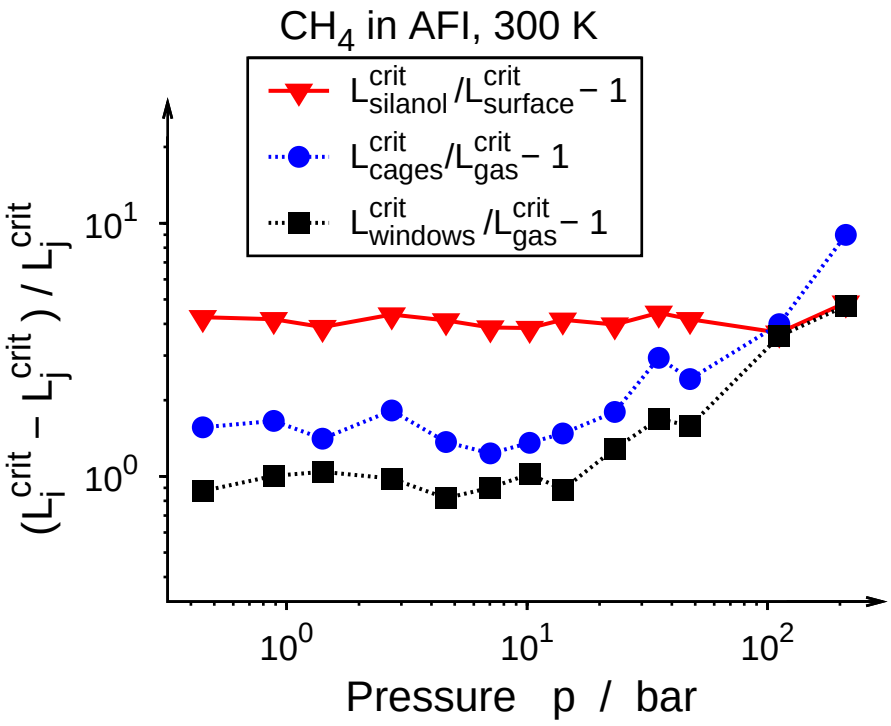

Figure 11: Relative differences between critical crystal lengths, as obtained from the simulations and the model that is based on the gas-phase flux. Additionally, an estimate of possible chemical barriers is given ($L^{\text{crit}}_{\text{silanol}}$) that is based on the results of Thompho *et al.*[22]